coatings

MDPI

Article

Interfacial Stability between High-Entropy $(La_{0.2}Yb_{0.2}Sm_{0.2}Eu_{0.2}Gd_{0.2})_2Zr_2O_7$ and Yttria-Stabilized Zirconia for Advanced Thermal Barrier Coating Applications

Guojie Yang [1], Chenbing Han [1], Ying Chen [2], Fangwei Guo [3], Jie Lu [3], Ming Zhou [1], Lirong Luo [3,*] and Xiaofeng Zhao [3,*]

[1] Faculty of Materials Science and Chemistry, China University of Geosciences, Wuhan 430074, China; 20181004002@cug.edu.cn (G.Y.); 1202210270@cug.edu.cn (C.H.); mingzh0728@outlook.com (M.Z.)
[2] Department of Materials, Henry Royce Institute, University of Manchester, Manchester M13 9PL, UK; ying.chen-2@manchester.ac.uk
[3] Shanghai Key Laboratory of Advanced High-Temperature Materials and Precision Forming, School of Materials Science and Engineering, Shanghai Jiao Tong University, Shanghai 200240, China; fwguo2014@sjtu.edu.cn (F.G.); lu-jie@sjtu.edu.cn (J.L.)
* Correspondence: lirongluo@yeah.net (L.L.); xiaofengzhao@sjtu.edu.cn (X.Z.); Tel./Fax: +86-21-5474-2561 (X.Z.)

Abstract: $(La_{0.2}Yb_{0.2}Sm_{0.2}Eu_{0.2}Gd_{0.2})_2Zr_2O_7$ (HEZ) has shown considerable promise as a novel thermal barrier coating material for temperatures exceeding 1300 °C. This study systematically investigates the interfacial stability of $(La_{0.2}Yb_{0.2}Sm_{0.2}Eu_{0.2}Gd_{0.2})_2Zr_2O_7$ with yttria-stabilized zirconia (YSZ), which is of paramount importance for its application in double-layer thermal barrier coatings. Our findings highlight that rare earth elements with a smaller radius diffuse more easily into the YSZ lattice, resulting in a broader diffusion zone. Simultaneously, the incorporation of rare earth elements into the YSZ lattice inhibits tetragonal-to-monoclinic phase transformation. Compared to $La_2Zr_2O_7$/YSZ, HEZ/YSZ demonstrates superior high-temperature stability, which could be attributed to the higher fracture toughness and lower thermal expansion coefficient of HEZ, the absence of t-m transformation and the formation of a continuous gradient diffusion layer that minimizes interface stress. This study offers a practical strategy for designing materials for durable double-layer thermal barrier coating systems.

Keywords: thermal barrier coating; high-entropy ceramics; rare earth zirconates; chemical stability; diffusion; interface

Citation: Yang, G.; Han, C.; Chen, Y.; Guo, F.; Lu, J.; Zhou, M.; Luo, L.; Zhao, X. Interfacial Stability between High-Entropy $(La_{0.2}Yb_{0.2}Sm_{0.2}Eu_{0.2}Gd_{0.2})_2Zr_2O_7$ and Yttria-Stabilized Zirconia for Advanced Thermal Barrier Coating Applications. *Coatings* **2024**, *14*, 269. https://doi.org/10.3390/coatings14030269

Academic Editor: Narottam P. Bansal

Received: 18 January 2024
Revised: 20 February 2024
Accepted: 21 February 2024
Published: 22 February 2024

1. Introduction

Rare earth zirconates ($RE_2Zr_2O_7$, RE = La~Yb) have been considered as promising materials for thermal barrier coating (TBC) due to their exceptional phase stability (maintaining stability above 1300 °C) and low thermal conductivity [1,2]. However, the practical application of these materials has been hampered by their low coefficient of thermal expansion (CTE) and inadequate fracture toughness [3,4]. To address these challenges, the concept of high entropy, inherited from the field of metal alloys, has been employed to improve the properties of rare earth zirconates [5–7]. High-entropy variants of these zirconates have demonstrated improved fracture toughness and phase stability, reduced thermal conductivity, increased high CTE and improved sintering resistance compared to their conventional single-component counterparts [8–10]. Consequently, high-entropy rare zirconates exhibit great potential as TBC materials [11–13]. Nonetheless, the chemical reactivity between these zirconates and Al_2O_3, which constitutes the primary component of the thermal growth oxide (TGO) layer, hinders their direct application as a single topcoat material on the bond coat [14]. Therefore, an yttria-stabilized zirconia (YSZ) buffer layer is typically employed, leading to the formation of a $RE_2Zr_2O_7$/YSZ double-layer

structure [15–18]. Chemical stability between $(5RE_{0.2})_2Zr_2O_7$ and YSZ is critical for the interface stability and longevity of the $(5RE_{0.2})_2Zr_2O_7$/YSZ double-layer system, an issue that warrants further investigation.

This study aims to comprehensively investigate the chemical stability of a high-entropy rare earth zirconate, namely $(La_{0.2}Yb_{0.2}Sm_{0.2}Eu_{0.2}Gd_{0.2})_2Zr_2O_7$ (HEZ), with YSZ. HEZ was selected for its advantageous properties, including low thermal conductivity (1.17 $W{\cdot}m^{-1}{\cdot}K^{-1}$ at 1500 °C), high CTE (10.39 × 10^{-6} K^{-1} from room temperature to 1500 °C), excellent sintering resistance and elevated fracture toughness (1.69 $MPa{\cdot}m^{1/2}$), as previously documented [19]. The HEZ/YSZ composite ceramic was prepared using the solid-state method, and its phase composition, microstructure and element distribution were analyzed and compared with those of $La_2Zr_2O_7$/YSZ after sintering at 1300 and 1500 °C for 10 and 100 h.

2. Experimental Section

The solid-state method was employed to synthesize $(La_{0.2}Yb_{0.2}Sm_{0.2}Eu_{0.2}Gd_{0.2})_2Zr_2O_7$ (HEZ), $La_2Zr_2O_7$ (LZ) and 8 wt.% yttria-stabilized zirconia (YSZ) materials. Raw materials, including rare-earth oxides RE_2O_3 (RE = La, Sm, Eu, Gd, Yb, 99.99%, Aladdin Reagent Co., Ltd., Shanghai, China), Y_2O_3 and ZrO_2 (99.99%, Aladdin Reagent Co., Ltd., Shanghai, China), were dried at 800 °C for 2 h to remove moisture and volatile contaminants before being weighed in stoichiometric ratios. Subsequently, the powders were mixed and ball-milled for 20 h using a high-energy ball mill to ensure the homogenous blending of the raw material powders for the subsequent sintering process. The resulting powders were dried, sieved and sintered at 1500 °C for 4 h for HEZ and LZ, and at 1250 °C for 4 h for YSZ. Composite materials HEZ/YSZ and LZ/YSZ were prepared by mixing equal masses of YSZ and HEZ or LZ powders. The mixture was pressed into disks with a diameter of 15 mm under a pressure of 100 MPa, followed by sintering in an air atmosphere at 1300 and 1500 °C for 10 and 100 h.

The phase composition of the as-sintered powders and composites was characterized using X-ray diffraction (XRD, Rigaku Smart lab SE, Tokyo, Japan) with a scanning range of 10–90° at a speed of 10°/min. The relative contents (A) of the tetragonal (T) phase, cubic (C) phase and monoclinic (M) phase of YSZ after high-temperature heat treatment were determined through the Lorenz fitting of the XRD pattern in the ranges of 27~32° and 72~76° using the following equation:

$$A_M = \frac{I_M(11\bar{1}) + I_M(111)}{I_M(11\bar{1}) + I_M(111) + I_{C,T}(111)} \quad (1)$$

$$A_T = \frac{(1 - A_M) \times (I_T(400) + I_T(004)}{I_T(400) + I_T(004) + I_C(400)} \quad (2)$$

$$A_C = 1 - (A_M + A_T) \quad (3)$$

where I is the integrated intensity of corresponding peaks. For microstructural and elemental analysis of the composites, scanning electron microscopy (SEM, FEI F50, Hillsboro, USA) was employed using the MIRA3 TESCAN instrument equipped with an energy-dispersive spectroscopy (EDS, FEI F50, Hillsboro, OR, USA) system. Prior to the SEM measurements, the composite surface was ground and polished.

3. Results

Figure 1 depicts the XRD patterns of the synthesized HEZ, LZ and YSZ powders, as well as the reference peaks of $RE_2Zr_2O_7$ (RE = La, Sm, Eu, Gd, Yb) obtained from ICDD/JCPDS cards for comparison. Both the HEZ and LZ powders exhibit a single pyrochlore (P) structure, as evidenced by the characteristic super-lattice (331) and (511) diffraction peaks [20]. Notably, the diffraction peaks of HEZ shift to higher angles compared to LZ, indicating a contraction in lattice parameters attributed to the decrease in the

effective ion radius. The YSZ powder presents a single tetragonal (T) structure without any impurity phases.

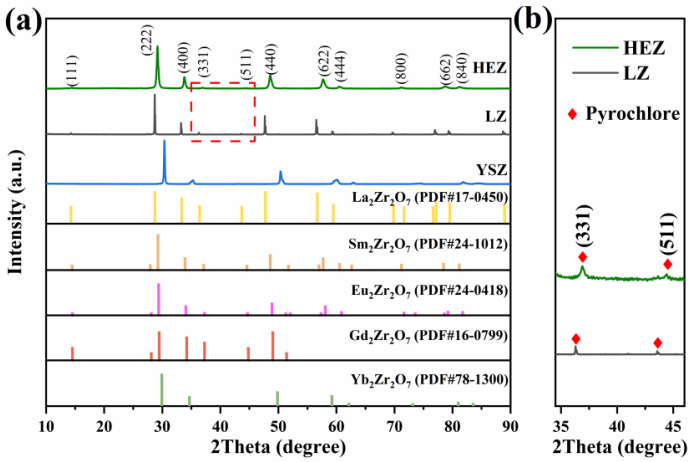

Figure 1. (**a**) XRD of the as-synthesized HEZ, LZ and YSZ powders and (**b**) partial enlarged view of the selected area in (**a**).

Figure 2a illustrates the XRD patterns of the LZ/YSZ and HEZ/YSZ composites after sintering at 1300 and 1500 °C for 10 and 100 h. The XRD patterns in the range of 27~32° and 72~76° are presented to provide a clear view of the YSZ phase evolution. In LZ/YSZ, after sintering at 1300 °C for 10 h, the YSZ is predominantly composed of tetragonal (T) and cubic (C) phases. With prolonged sintering, a minor amount of monoclinic (M) phase emerges after 100 h, evident from characteristic $(11\bar{1})$ and (111) peaks [21]. Elevating the sintering temperature to 1500 °C results in the occurrence of a monoclinic phase even after 10 h. This indicates the transformation of YSZ from a tetragonal (T) to a monoclinic (M) phase, which is accompanied by a 3~5% volume expansion and induces local compressive stress [22]. The characteristic peaks of the T-YSZ in the range of 72~75° almost disappear after a 100 h of sintering at 1500 °C, suggesting complete transformation to the cubic phase.

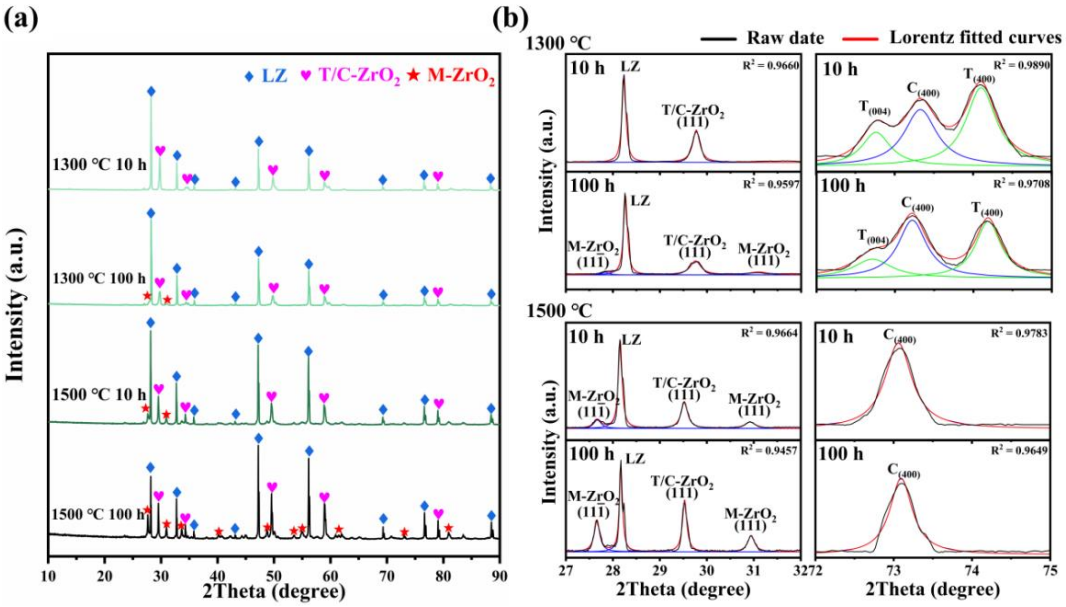

Figure 2. (**a**) XRD patterns of LZ/YSZ after sintering at 1300 and 1500 °C for 10 and 100 h, and (**b**) corresponding enlarged view in the range of 27~32° and 72~76°; the black lines represent the raw data, while the other lines represent Lorentz fitted curves.

Figure 3a illustrates the phase evolution of HEZ/YSZ composites after sintering at 1300 and 1500 °C for 10 and 100 h. It is obvious that the tetragonal (T) YSZ in HEZ/YSZ composites undergoes a transformation into the cubic phase with prolonged sintering time and temperature, and no peaks corresponding to monoclinic (M) YSZ are observed. Additionally, the peaks exhibit a shift towards lower angles, indicative of lattice expansion. Another significant feature is the decreasing intensity of the HEZ with the pyrochlore phase marked with HEZ-P in Figure 3b, with the phase nearly disappearing after sintering at 1500 °C for 100 h. Meanwhile, a new peak at 2θ of 29.7° occurs between the existing peaks of HEZ-P and (111) the peaks of YSZ, which is identified as HEZ-F with a fluorite (cubic) phase according to the XRD analysis.

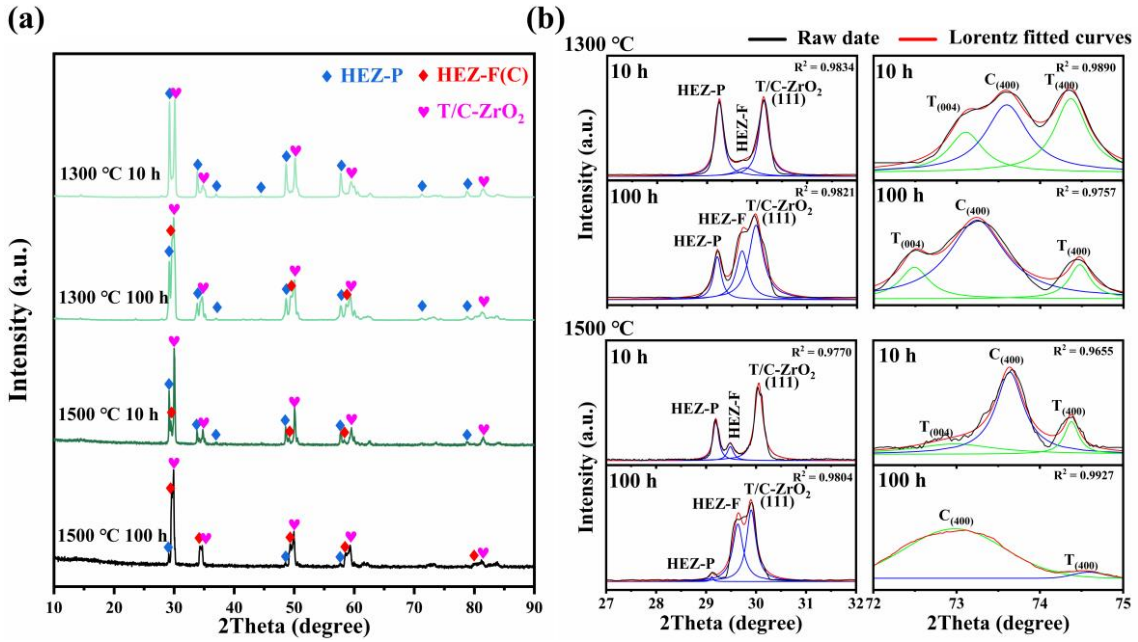

Figure 3. (**a**) XRD patterns of HEZ/YSZ after sintering at 1300 and 1500 °C for 10 and 100 h, and (**b**) corresponding enlarged view in the ranges of 27~32° and 72~76°. The black, green, blue and red lines represent raw data and the peaks of the tetragonal, cubic and combined curves of the two phases based on Lorentz fitting, respectively.

For a quantitative analysis of the phase evolution of YSZ in LZ/YSZ and HEZ/YSZ composites, the phase content of YSZ was determined from the XRD results and is presented in Figure 4. It is evident that the content of T-YSZ in LZ/YSZ decreases from 64.13% to 37.96%, while the content of the monoclinic phase increases to 32.39% with an increase in sintering time from 10 to 100 h at 1300 °C. Upon elevating the sintering temperature to 1500 °C, the T-YSZ is almost decomposed into cubic (C) and monoclinic (M) phases. Meanwhile, the content of the monoclinic (M) phase increases with both sintering time and temperature. In contrast, in the case of HEZ/YSZ, the T-YSZ transforms into the cubic (C) phase and no monoclinic (M) phase is detected. This observed difference is related to variations in elemental diffusion between these two samples.

To analyze the elemental diffusion behavior in LZ/YSZ and HEZ/YSZ, the surface microstructure and elemental mapping at the interface were characterized using BSE and EDS, as presented in Figures 5 and 6. Figure 5 reveals the presence of numerous pores in both composites, with a non-uniform distribution primarily concentrated in the rare earth zirconate (LZ and HEZ) regions. This non-uniform pore distribution could be attributed to the higher sintering resistance of rare earth zirconates compared to YSZ. At higher magnification, microcracks are visible in LZ, while none are present in HEZ. Additionally, the boundaries between the LZ and YSZ boundaries are sharp, whereas those between HEZ and YSZ are gradual and diffuse. The elemental distribution around the interface of the samples is shown in Figure 6, indicating an expansion in the element diffusion region as

temperature increases, particularly evident in HEZ/YSZ. Table 1 summarizes the element composition at the marked position in Figure 6, where the rare earth superposition is labeled "RE". Several notable observations are made: (1) The diffusion of Y^{3+} is more pronounced in LZ/YSZ than in HEZ/YSZ. This could be related to the severe lattice distortion of HEZ, which hinders the inward diffusion of Y^{3+} [23]. (2) RE diffuses faster into YSZ than Y^{3+} diffuses into HEZ (or LZ) [24,25]. (3) The RE content in the diffusion region of HEZ/YSZ increases as the ionic radius (as shown in Table 1) decreases.

Line scanning was performed along the path indicated by the black arrow in Figure 6 to determine the diffusion zone width of the samples, with the corresponding element distribution illustrated in Figure 7. The diffusion zone was assessed based on the concentration of La^{3+}, found to be higher than in the bulk LZ or HEZ but lower than in the bulk YSZ. After sintering at 1500 °C for 10 and 100 h, the diffusion zone widths of LZ/YSZ are 1.2 ± 0.2 μm and 2.2 ± 0.3 μm, respectively. These values are significantly smaller than those observed in HEZ/YSZ, which recorded diffusion zone widths of 4.5 ± 0.5 μm and 6.5 ± 0.5 μm after the same sintering periods. This demonstrates significantly more rapid elemental diffusion in HEZ/YSZ, with the rate increasing as sintering time increases.

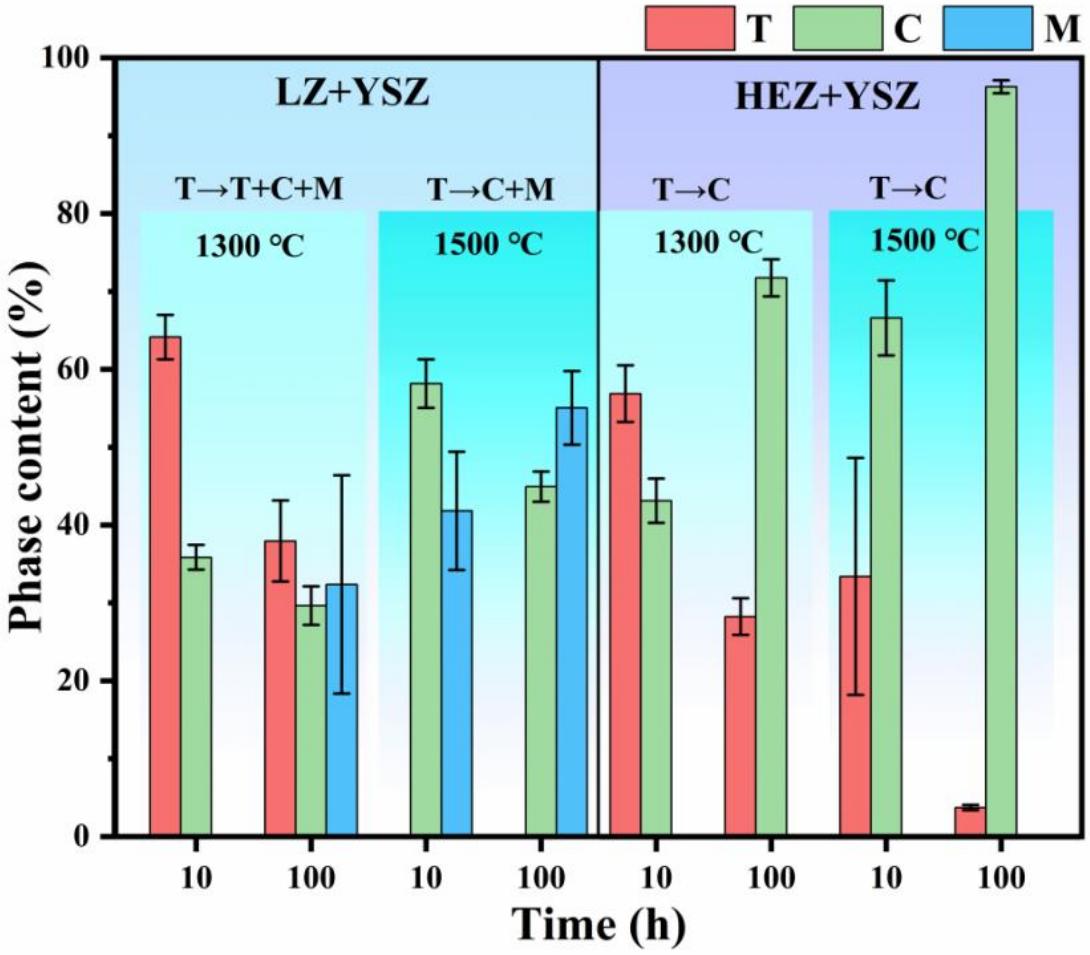

Figure 4. Phase composition and content of YSZ in LZ/YSZ and HEZ/YSZ composites after sintering at 1300 and 1500 °C for 10 and 100 h.

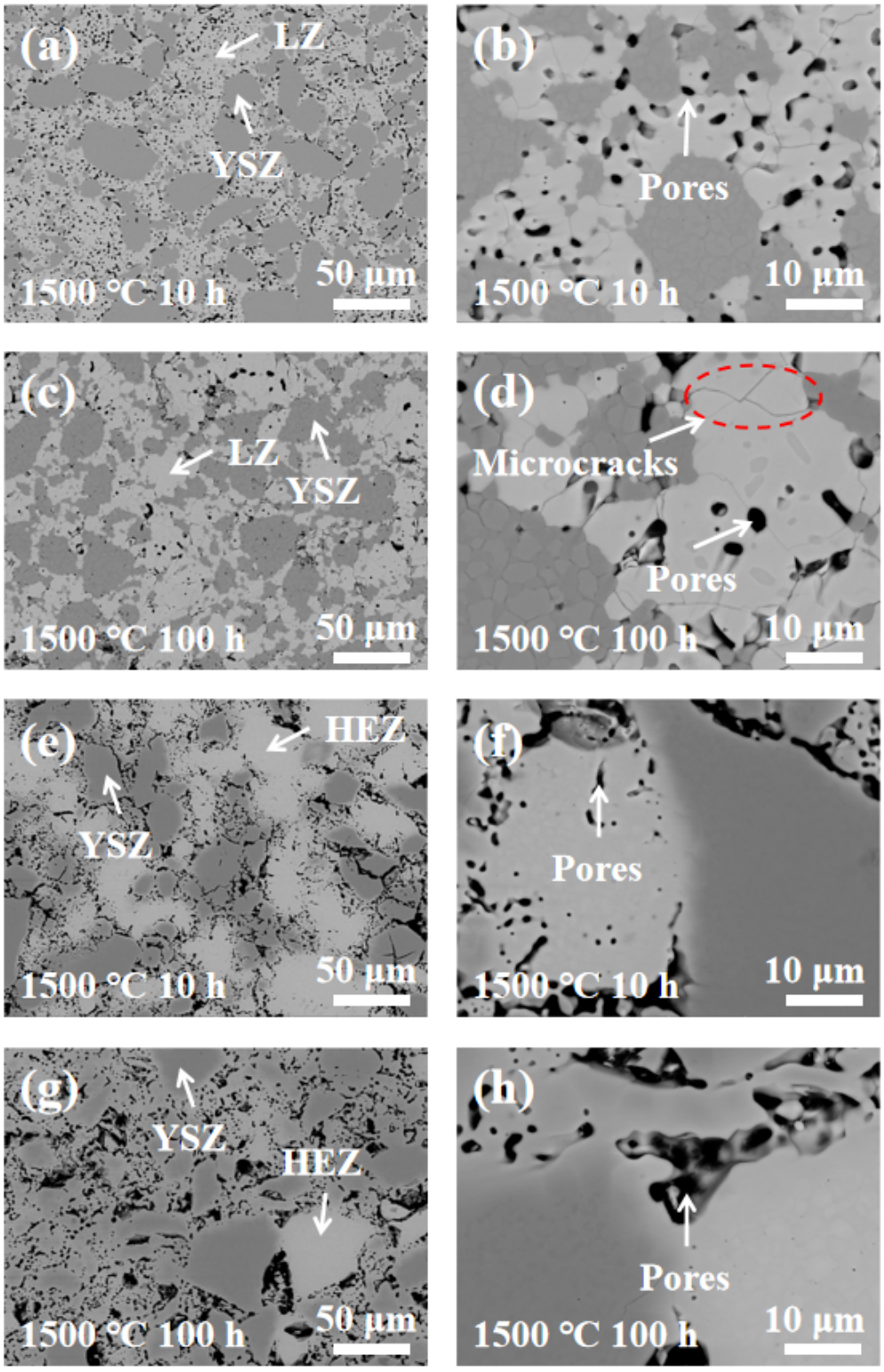

Figure 5. BSE images of (**a**–**d**) LZ/YSZ and (**e**–**h**) HEZ/YSZ after sintering at 1500 °C for 10 and 100 h.

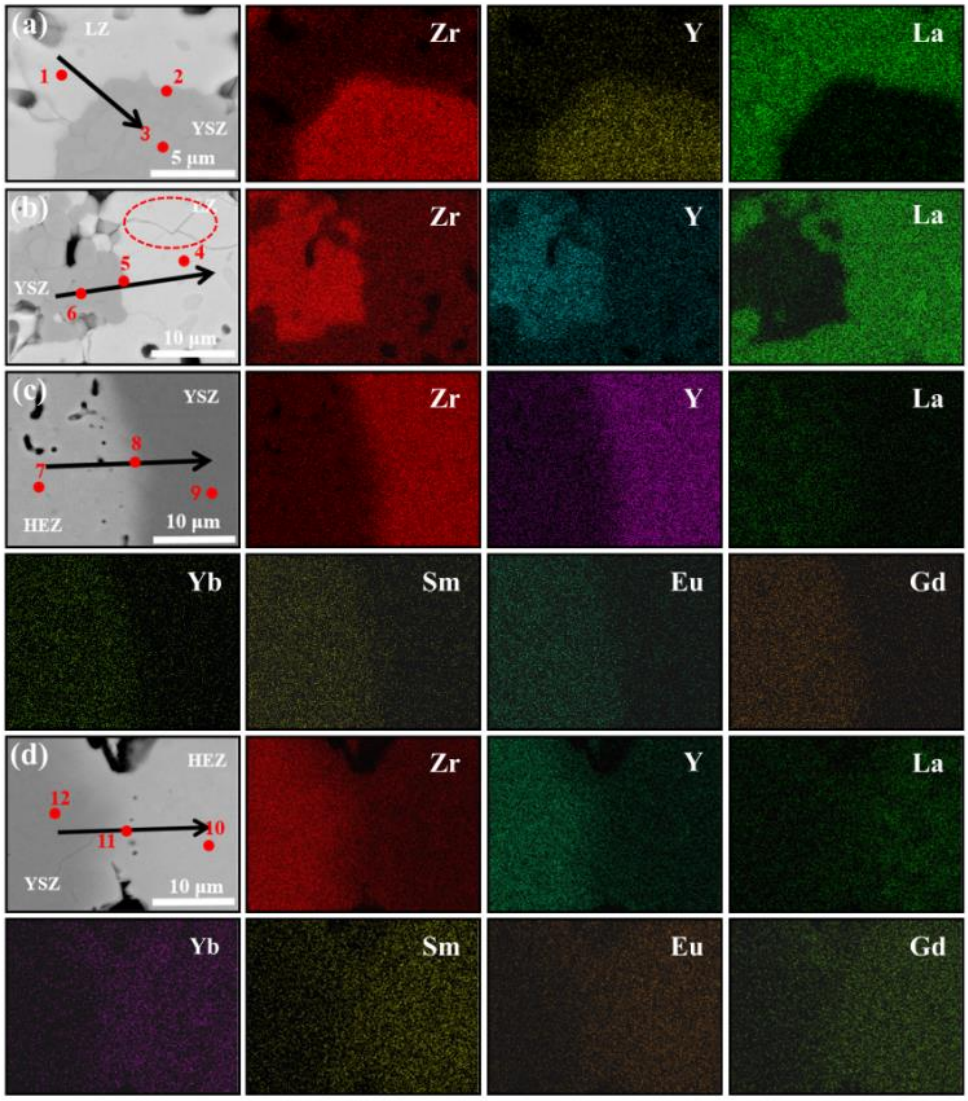

Figure 6. Backscattered electron (BSE) images and corresponding EDS mapping around the phase boundary of (**a**,**b**) LZ/YSZ and (**c**,**d**) HEZ/YSZ after sintering at 1500 °C for 10 and 100 h, respectively. The red dotted circle represents the typical area (YSZ, HEZ or LZ, and the interface).

Table 1. Element composition of the points marked in Figure 6 (at.%) and the ion radius corresponding to each element.

		O	Y	Zr	La	Sm	Eu	Gd	Yb	RE
Ionic Radius (Å)			**1.019**	**0.72**	**1.16**	**1.079**	**1.066**	**1.053**	**0.985**	
LZ/YSZ (1500 °C 10 h)	1 (LZ)	59.6(2)	0.6(2)	20.9(4)	18.9(4)	-	-	-	-	-
	2 (Interface)	60.3(1)	1.1(2)	36.0(5)	2.7(4)	-	-	-	-	-
	3 (YSZ)	61.2(0)	3.8(2)	33.6(3)	1.4(1)	-	-	-	-	-
LZ/YSZ (1500 °C 100 h)	4 (LZ)	60.2(1)	0.9(4)	20.4(2)	18.5(1)	-	-	-	-	-
	5 (Interface)	59.6(1)	1.0(2)	34.2(1)	5.0(2)	-	-	-	-	-
	6 (YSZ)	62.0(4)	4.2(1)	32.2(2)	1.6(3)	-	-	-	-	-
HEZ/YSZ (1500 °C 10 h)	7 (HEZ)	58.7(1)	0.0(3)	25.0(4)	2.4(3)	3.2(2)	3.4(0)	3.6(3)	3.7(0)	16.3
	8 (Interface)	61.0(1)	2.7(0)	29.2(3)	1.2(1)	1.3(2)	1.3(2)	1.4(2)	1.8(1)	7.1
	9 (YSZ)	60.8(5)	3.5(1)	32.8(4)	0.7(2)	0.6(3)	0.5(2)	0.6(0)	0.6(2)	3.1

Table 1. *Cont.*

		O	Y	Zr	La	Sm	Eu	Gd	Yb	RE
Ionic Radius (Å)			**1.019**	**0.72**	**1.16**	**1.079**	**1.066**	**1.053**	**0.985**	
HEZ/YSZ (1500 °C 100 h)	10 (HEZ)	58.9(2)	0.0(0)	21.5(2)	5.3(5)	4.2(3)	3.9(1)	3.8(4)	2.5(3)	19.6
	11 (Interface)	59.0(3)	0.1(2)	25.2(4)	2.2(3)	2.9(0)	3.1(2)	3.3(4)	4.1(2)	15.6
	12 (YSZ)	62.1(2)	3.0(0)	28.8(1)	1.1(3)	1.2(3)	1.2(3)	1.2(3)	1.5(1)	6.1

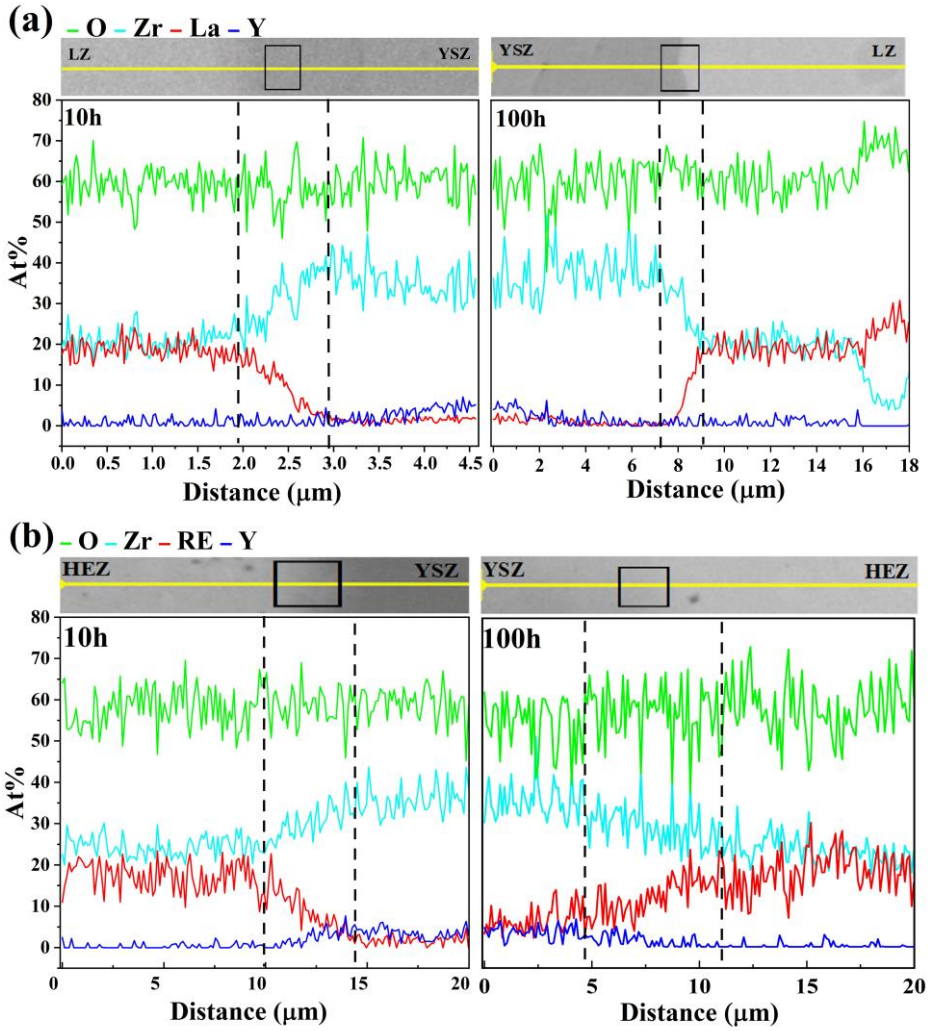

Figure 7. Elemental distribution along the path marked by an arrow in Figure 6: (**a**) LZ/YSZ and (**b**) HEZ/YSZ after sintering at 1500 °C for 10 (**left**) and 100 h (**right**), respectively.

4. Discussion

It has been established that HEZ/YSZ exhibits a significantly larger elemental diffusion zone compared to LZ/YSZ, particularly evident after sintering at 1500 °C. The boundary between LZ and YSZ is well-defined, while HEZ and YSZ form a dense and continuous reaction zone, accompanied by a phase transformation of YSZ. In this section, RE^{3+} diffusion behavior and its impact on YSZ phase transformation are examined.

4.1. RE Diffusion

The element diffusion zone between the rare earth zirconates and YSZ is presented in both samples. The similar crystal structures of rare earth zirconates (cubic and tetragonal) and YSZ facilitate element interdiffusion between the two phases [26]. However, the

elemental diffusion zone in HEZ/YSZ is significantly wider than in LZ/YSZ. RE^{3+} ions with smaller radii diffuse more easily into the YSZ lattice, a finding supported by the EDS results. This is attributed to their smaller radius difference with Zr^{4+}, making it easier for them to replace Zr^{4+} and form a single-phase solid solution. In contrast, LZ/YSZ exhibits a clearly defined boundary between the two phases, and the diffusion of Y^{3+} into LZ is much easier than into HEZ. This discrepancy could be related to the severe lattice distortion of HEZ, which retards the inward diffusion of Y^{3+}.

4.2. Phase Evolution

The phase transformation of YSZ in HEZ/YSZ differs from that of LZ/YSZ. This can be elucidated using the phase diagram of ZrO_2-$REO_{1.5}$, depicted in Figure 8 [27], where the red dashed line represents the annealing temperature of the material at 1500 °C. The blue and yellow arrows represent the phase evolution of LZ/YSZ and HEZ/YSZ after sintering. For the LZ/YSZ composite, La^{3+} diffuses into the T-ZrO_2 lattice and reaches its solubility limit (less than 0.5 mol%), leading to a transformation from T to cubic (C) [28]. However, due to the significant radius difference with Zr^{4+}, the content of La^{3+} in YSZ is very low even at a sintering temperature of 1500 °C. Upon cooling, the T-ZrO_2 decomposes into the M+C phase. The content of Y^{3+} in LZ is less than 1%, and LZ preserves the pyrochlore structure.

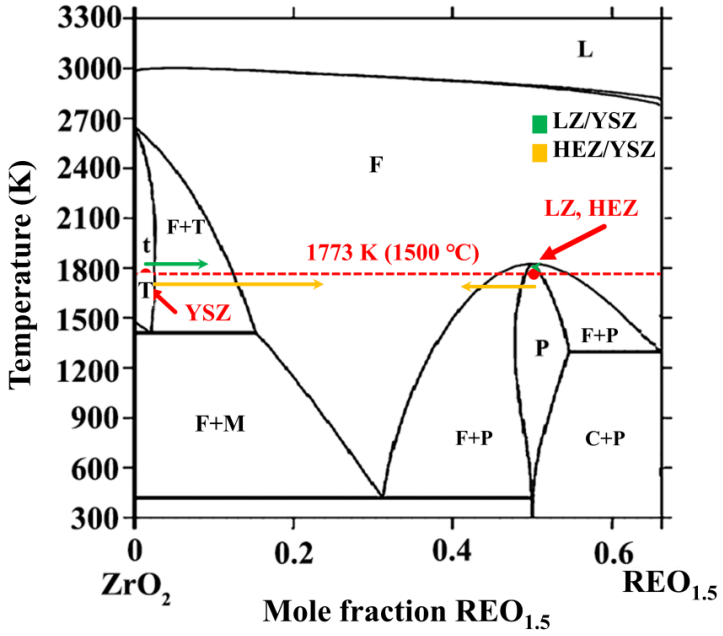

Figure 8. Phase diagram of ZrO_2-$REO_{1.5}$. The composition evolution of YSZ and rare earth zirconate, including LZ (green) and HEZ (yellow), are marked with arrows. The red dashed line represents a temperature of 1500 °C.

In the case of HEZ/YSZ, cubic phases are presented after sintering at 1500 °C for 10 h. This is attributed to RE^{3+} ions with small radii, such as Yb^{3+}, easily entering the T-ZrO_2 lattice. According to the EDS results, the proportion of stabilizers in YSZ was determined, defined as the ratio of stabilizer ions (including Y^{3+} and RE^{3+}) to all cations (including Y^{3+}, RE^{3+} and Zr^{4+}). This value was calculated to be 16.75 % for point 9, exceeding the solubility limit and driving the phase transformation from T to C. With an increase in sintering time of 100 h, the stabilizer content proportion in YSZ (point 12) rises to 24.01%, causing an almost complete transformation of T-YSZ into the C phase. HEZ transitions from a single pyrochlore (P) phase into a mixed pyrochlore and fluorite (or cubic) phase as the molar ratio of RE^{3+}/Zr^{4+} falls from 50% to 42%. Element diffusion could also contribute to the formation of the mixing phase of HEZ, as elements with small radii, like Yb^{3+}, can

rapidly enter the diffusion zone. In this region, as the radius ratio between RE^{3+} and Zr^{4+} falls below the threshold value (1.46), the rare earth zirconates transform into a fluorite (cubic, C) structure. This is supported by the XRD results, showing the emergence of a new phase with a fluorite structure with prolonged sintering time. The element diffusion and phase evolution of the two samples at 1500 °C at the boundary are proposed and schematically illustrated in Figure 9. The LZ/YSZ system has a relatively narrow transition zone. Due to the diffusion of Y^{3+}, the content of stabilizer ions in YSZ decreases, leading to ZrO_2 undergoing a T-M phase transition, thereby reducing the stability of YSZ in high-temperature environments. In contrast, the HEZ/YSZ system features a wide transition zone. Due to the diffusion of RE^{3+} into the YSZ lattice, the concentration of stabilizer ions increases, hindering the T-M phase transformation of ZrO_2.

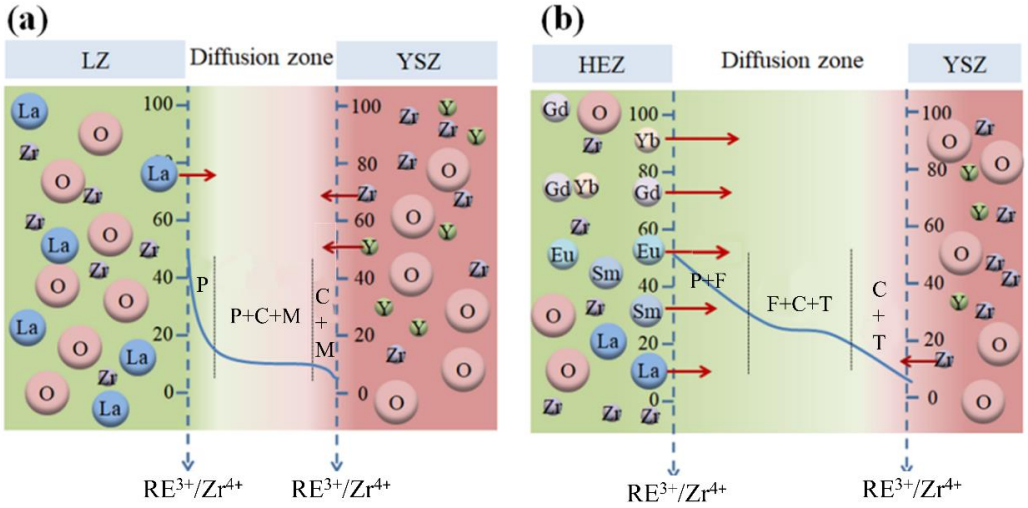

Figure 9. Schematics of element diffusion and phase evolution at the boundary of (**a**) LZ/YSZ and (**b**) HEZ/YSZ after sintering at 1500 °C; the vertical axis is expressed as the percentage of the cation ratio.

4.3. Implication of TBC Applications

According to the aforementioned discussion, it is evident that the chemical compatibility of LZ with YSZ surpasses that of HEZ, primarily due to reduced elemental diffusion and a smaller diffusion zone. Nonetheless, it is crucial to note that small cracks develop in LZ after sintering at elevated temperatures, while no cracks are observed in HEZ. Several potential reasons account for this observation: (1) the fracture toughness of HEZ, measured at 1.69 $MPa{\cdot}m^{1/2}$, is 22.5% higher than that of LZ, which impedes the formation of cracks [29]; (2) HEZ exhibits a CTE of 10.39×10^{-6} K^{-1}, which is 16.6% larger than that of LZ (8.91×10^{-6} K^{-1}) [19], making it comparable to YSZ and resulting in less misfit stress; (3) local stress concentration caused by the T-M transformation in LZ/YSZ, accompanied by 3~5% volume expansion, eventually leads to crack initiation and propagation; (4) the higher porosity in HEZ than that of LZ due to its higher sintering resistance may provide more free space to alleviate the phase transformation strain; (5) a continuous gradient layer is generated at the HEZ/YSZ boundary, potentially relieving the interface stress. Despite having more element diffusion, HEZ/YSZ may demonstrate superior interfacial stability compared to LZ/YSZ, indicating promising prospects for long-term application in double-layer TBCs. The thermal cycling life and failure behaviors of the HEZ/YSZ double-layer coating will be systematically examined in our upcoming work.

5. Conclusions

$(La_{0.2}Yb_{0.2}Sm_{0.2}Eu_{0.2}Gd_{0.2})_2Zr_2O_7$ (HEZ) and $La_2Zr_2O_7$ (LZ) were synthesized via a solid-state reaction, and their chemical stability with YSZ was comparatively studied.

It was observed that RE^{3+} with a smaller radius, such as Yb^{3+}, can easily enter the YSZ lattice and stabilize the tetragonal and cubic (fluorite) phases, thereby prohibiting

tetragonal-to-monoclinic phase transformation. The diffusion of Y^{3+} into LZ was found to be much easier than into HEZ, possibly due to the severe lattice distortion of HEZ, which impedes the inward diffusion of Y^{3+}. Despite the rapid element diffusion, HEZ exhibited higher high-temperature stability than LZ. This can be attributed to its high fracture toughness and low thermal expansion coefficient, the absence of T-M transformation and the formation of a continuous gradient diffusion layer capable of relieving interface stress. Consequently, HEZ holds great promise for long-term application in double-layer TBC due to its superior comprehensive properties and excellent high-temperature stability with YSZ.

Author Contributions: G.Y.: Conceptualization, Methodology, Investigation, Data curation, Writing—original draft, Writing—review & editing. C.H.: Investigation, Data curation, Writing-review & editing. Y.C.: Investigation, Data curation, Writing—review & editing. F.G.: Investigation, Data curation, Writing—review & editing. J.L.: Data curation, Writing—review & editing. M.Z.: Data curation, Writing—review & editing. L.L.: Conceptualization, Methodology, Supervision, Writing—review & editing. X.Z.: Methodology, Supervision, Writing—review & editing. All authors have read and agreed to the published version of the manuscript.

Funding: National Natural Science Foundation of China (52101101).

Institutional Review Board Statement: Not applicable.

Informed Consent Statement: Not applicable.

Data Availability Statement: Data available on request from the authors.

Acknowledgments: The authors wish to thank the Science and Technology Commission of the CPC Central Military Commission for their support.

Conflicts of Interest: The authors declare no conflict of interest.

References

1. Karabaş, M. Production and characterization of Nd and Dy doped lanthanum zirconate-based thermal barrier coatings. *Surf. Coat. Technol.* **2020**, *394*, 125864. [CrossRef]
2. Yang, J.; Shahid, M.; Zhao, M.; Feng, J.; Wan, C.; Pan, W. Physical properties of $La_2B_2O_7$(B Zr, Sn, Hf and Ge) pyrochlore: First-principles calculations. *J. Alloys Compd.* **2016**, *663*, 834–841. [CrossRef]
3. Bobzin, K.; Bagcivan, N.; Brögelmann, T.; Yildirim, B. Influence of temperature on phase stability and thermal conductivity of single- and double-ceramic-layer EB–PVD TBC top coats consisting of 7YSZ, $Gd_2Zr_2O_7$ and $La_2Zr_2O_7$. *Surf. Coat. Technol.* **2013**, *237*, 56–64. [CrossRef]
4. Lutique, S.; Javorskỳ, P.; Konings, R.; Krupa, J.-C.; van Genderen, A.; van Miltenburg, J.; Wastin, F. The low-temperature heat capacity of some lanthanide zirconates. *J. Chem. Thermodyn.* **2004**, *36*, 609–618. [CrossRef]
5. Xiang, H.; Xing, Y.; Dai, F.-Z.; Wang, H.; Su, L.; Miao, L.; Zhang, G.; Wang, Y.; Qi, X.; Yao, L.; et al. High-entropy ceramics: Present status, challenges, and a look forward. *J. Adv. Ceram.* **2021**, *10*, 385–441. [CrossRef]
6. George, E.P.; Curtin, W.A.; Tasan, C.C. High Entropy Alloys: A Focused Review of Mechanical Properties and Deformation Mechanisms. *Acta Mater.* **2020**, *188*, 435–474. [CrossRef]
7. Rost, C.M.; Sachet, E.; Borman, T.; Moballegh, A.; Dickey, E.C.; Hou, D.; Jones, J.L.; Curtarolo, S.; Maria, J.-P. Entropy-stabilized oxides. *Nat. Commun.* **2015**, *6*, 8485. [CrossRef] [PubMed]
8. Zhang, R.-Z.; Reece, M.J. Review of high entropy ceramics: Design, synthesis, structure and properties. *J. Mater. Chem. A* **2019**, *7*, 22148–22162. [CrossRef]
9. Zhou, L.; Li, F.; Liu, J.-X.; Hu, Q.; Bao, W.; Wu, Y.; Cao, X.; Xu, F.; Zhang, G.-J. High-entropy thermal barrier coating of rare-earth zirconate: A case study on $(La_{0.2}Nd_{0.2}Sm_{0.2}Eu_{0.2}Gd_{0.2})_2Zr_2O_7$ prepared by atmospheric plasma spraying. *J. Eur. Ceram. Soc.* **2020**, *40*, 5731–5739. [CrossRef]
10. Wang, J.; Wu, F.; Zou, R.; Wu, Y.; Gan, M.; Feng, J.; Chong, X. High-entropy ferroelastic rare-earth tantalite ceramic: $(Y_{0.2}Ce_{0.2}Sm_{0.2}Gd_{0.2}Dy_{0.2})TaO_4$. *J. Am. Ceram. Soc.* **2021**, *104*, 5873–5882. [CrossRef]
11. Luo, X.; Luo, L.; Zhao, X.; Cai, H.; Duan, S.; Xu, C.; Huang, S.; Jin, H.; Hou, S. Single-phase rare-earth high-entropy zirconates with superior thermal and mechanical properties. *J. Eur. Ceram. Soc.* **2022**, *42*, 2391–2399. [CrossRef]
12. Zhao, Z.; Xiang, H.; Dai, F.-Z.; Peng, Z.; Zhou, Y. $(La_{0.2}Ce_{0.2}Nd_{0.2}Sm_{0.2}Eu_{0.2})_2Zr_2O_7$: A novel high-entropy ceramic with low thermal conductivity and sluggish grain growth rate. *J. Mater. Sci. Technol.* **2019**, *35*, 2647–2651. [CrossRef]
13. Liu, D.; Wang, Y.; Zhou, F.; Xu, B.; Lv, B. A novel high-entropy $(Sm_{0.2}Eu_{0.2}Tb_{0.2}Dy_{0.2}Lu_{0.2})_2Zr_2O_7$ ceramic aerogel with ultralow thermal conductivity. *Ceram. Int.* **2021**, *47*, 29960–29968. [CrossRef]
14. Leckie, R.; Krämer, S.; Rühle, M.; Levi, C. Thermochemical compatibility between alumina and ZrO_2–$GdO_{3/2}$ thermal barrier coatings. *Acta Mater.* **2005**, *53*, 3281–3292. [CrossRef]

15. Karaoglanli, A.C.; Doleker, K.M.; Ozgurluk, Y. Interface failure behavior of yttria stabilized zirconia (YSZ), $La_2Zr_2O_7$, $Gd_2Zr_2O_7$, YSZ/$La_2Zr_2O_7$ and YSZ/$Gd_2Zr_2O_7$ thermal barrier coatings (TBCs) in thermal cyclic exposure. *Mater. Charact.* **2020**, *159*, 110072. [CrossRef]
16. Mahade, S.; Curry, N.; Björklund, S.; Markocsan, N.; Nylén, P. Failure analysis of $Gd_2Zr_2O_7$/YSZ multi-layered thermal barrier coatings subjected to thermal cyclic fatigue. *J. Alloys Compd.* **2016**, *689*, 1011–1019. [CrossRef]
17. Mahade, S.; Curry, N.; Björklund, S.; Markocsan, N.; Nylén, P. Thermal conductivity and thermal cyclic fatigue of multilayered $Gd_2Zr_2O_7$/YSZ thermal barrier coatings processed by suspension plasma spray. *Surf. Coat. Technol.* **2015**, *283*, 329–336. [CrossRef]
18. Mensah, P.F.; Diwan, R.; Nandikolla, S.; Coker, O.; Sahoo, P. Thermo-Mechanical Study of the Role of $Gd_2Zr_2O_7$ (GZ) in Improving Life of YSZ and GZ Double Layered Thermal Barrier Coatings. In Proceedings of the ASME 2012 International Mechanical Engineering Congress and Exposition, Houston, TX, USA, 9–15 November 2012; pp. 3083–3088.
19. Luo, X.; Huang, R.; Xu, C.; Huang, S.; Hou, S.; Jin, H. Designing high-entropy rare-earth zirconates with tunable thermophysical properties for thermal barrier coatings. *J. Alloys Compd.* **2022**, *926*, 166714. [CrossRef]
20. Shimamura, K.; Arima, T.; Idemitsu, K.; Inagaki, Y. Thermophysical properties of rare-earth-stabilized zirconia and zirconate pyrochlores as surrogates for actinide-doped zirconia. *Int. J. Thermophys.* **2007**, *28*, 1074–1084. [CrossRef]
21. Xu, Z.; He, L.; Zhong, X.; Zhang, J.; Chen, X.; Ma, H.; Cao, X. Effects of Y_2O_3 addition on the phase evolution and thermophysical properties of lanthanum zirconate. *J. Alloys Compd.* **2009**, *480*, 220–224. [CrossRef]
22. Aruna, S.; Balaji, N.; Rajam, K. Phase transformation and wear studies of plasma sprayed yttria stabilized zirconia coatings containing various mol% of yttria. *Mater. Charact.* **2011**, *62*, 697–705. [CrossRef]
23. Zhu, J.; Meng, X.; Zhang, P.; Li, Z.; Xu, J.; Reece, M.J.; Gao, F. Dual-phase rare-earth-zirconate high-entropy ceramics with glass-like thermal conductivity. *J. Eur. Ceram. Soc.* **2021**, *41*, 2861–2869. [CrossRef]
24. Li, F.; Zhou, L.; Liu, J.-X.; Liang, Y.; Zhang, G.-J. High-entropy pyrochlores with low thermal conductivity for thermal barrier coating materials. *J. Adv. Ceram.* **2019**, *8*, 576–582. [CrossRef]
25. Wierzba, B. The Kirkendall Effect and Multi-component Diffusion Simulations. *High Temp. Mater. Process.* **2016**, *36*, 447–451. [CrossRef]
26. Liu, X.; Che, J.; Yi, H.; Liang, G. Chemical compatibility between $Ln_2Zr_2O_7$ (Ln = Nd, Sm, Gd) and tetragonal yttria stabilized zirconia after annealing at high temperatures. *Mater. Lett.* **2019**, *234*, 159–162. [CrossRef]
27. Fabrichnaya, O.; Wang, C.; Zinkevich, M.; Aldinger, F.; Levi, C.G. Phase equilibria and thermodynamic properties of the ZrO_2-$GdO_{1.5}$-$YO_{1.5}$ system. *J. Phase Equilibria Diffus.* **2005**, *26*, 591–604. [CrossRef]
28. Andrievskaya, E.; Kornienko, O.; Bykov, A.; Sameliuk, A. Phase Equilibria in the ZrO_2–La2O_3–Gd_2O_3 System at 1600 °C. *Sov. Powder Met. Met. Ceram.* **2020**, *58*, 714–724. [CrossRef]
29. Guo, X.; Li, L.; Park, H.-M.; Knapp, J.; Jung, Y.-G.; Zhang, J. Mechanical Properties of Layered $La_2Zr_2O_7$ Thermal Barrier Coatings. *J. Therm. Spray Technol.* **2018**, *27*, 581–590. [CrossRef]